

HELIOSEISMIC IMAGING OF THE FAR SIDE AND THE INTERIOR

D. C. Braun and C. Lindsey

NorthWest Research Associates, Colorado Research Associates Division, 3380 Mitchell Ln, Boulder, Colorado, 80301, USA

ABSTRACT

Helioseismic holography is a highly efficient and flexible procedure with a wide range of utility, from mapping sound wave travel times over the entire far solar hemisphere to imaging small scale scatterers and flows beneath solar active regions. Seismic images covering the entire far hemisphere of the Sun have been constructed using data from the recently upgraded Global Oscillation Network Group (GONG+) network and compare favorably with those made using simultaneous data from the Michelson Doppler Imager (MDI) onboard the *Solar and Heliospheric Observer (SOHO)*. We are also continuing our comprehensive exploration of diffraction-limited seismic imaging of active regions. We have recently extended our applications of helioseismic holography to include Doppler diagnostics of active regions and quiet Sun. A major finding presented here is that the horizontal velocity field in supergranules and sunspot moats appears to be concentrated at the surface. Another recent, but vital, contribution to local helioseismology has been a study of what is termed the “showerglass effect”. Magnetic fields in the photosphere produce large, local amplitude and phase perturbations to the observed acoustic wave field which may be quantified and removed prior to the holographic computations. Removal of the showerglass from local helioseismic images of active regions is proving to be a crucial step in the detection of compact subsurface scatterers.

Key words: local helioseismology; holography; active regions; supergranulation; farside.

1. INTRODUCTION

The basic principle of what we call helioseismic holography is the phase-coherent reconstruction of the acoustic field within the solar interior from p -mode disturbances observed on the surface. The acoustic field at the surface, observed over a limited region P , called the pupil, is computationally regressed through the solar interior to a focal point at

some distant location to express the acoustic egression and ingression. The egression and ingression are incomplete, but coherent, estimates of the acoustic disturbances propagating out of and into the focal point, respectively. In a “space-frequency” context, the egression and ingression are computed by integrals of the form:

$$H_{\pm}(\mathbf{r}, z, \nu) = \int_P d^2\mathbf{r}' G_{\pm}(\mathbf{r}, \mathbf{r}', z, \nu) \psi(\mathbf{r}', \nu) \quad (1)$$

where H_+ and H_- are the monochromatic egression and ingression, and ψ is the local acoustic disturbance at temporal frequency ν . G_+ and G_- are Green’s functions that express how a monochromatic point disturbance at a position \mathbf{r}' on the surface propagates backwards and forwards in time to the focus at \mathbf{r} and depth z respectively. A recent summary of many technical aspects of helioseismic holography is given by Lindsey & Braun (2000b). Our goal here is to report on progress in the development and application of “phase-correlation” seismic holography, which offers an appraisal of the phase shifts due to refractive and Doppler perturbations in the solar interior. A review of the scientific results achieved from earlier explorations in the domain of “acoustic power holography” may be found in Braun & Lindsey (2000a).

In section 2 below, we compare phase-correlation images, sensitive to travel-time perturbations, made from simultaneous data from the GONG+ network and the MDI instrument on *SOHO*, to assess the utility of the GONG+ images for local helioseismology, including farside imaging. In section 3, we report results obtained from Doppler-sensitive holographic computations from MDI observations. Depth-sensitivity of our phase-correlation computations is achieved by considering imaging configurations like that shown in Figure 1. In the final section, we summarize recent progress in understanding and correcting the phase and amplitude perturbations introduced locally to the surface wave field by magnetic regions, which act as an acoustic “showerglass”.

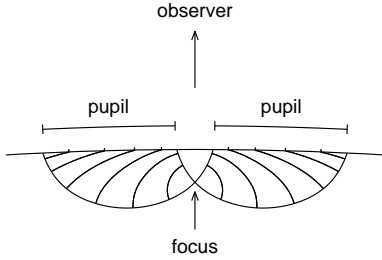


Figure 1. Seismic imaging with the focus placed at a depth below the solar surface. Here, the radiation sampled by the pupil illuminates the focal point from angles inclined up to $\pm 45^\circ$ from the horizontal direction. This configuration allows the construction of seismic images with the maximum possible horizontal resolution.

2. GONG+/MDI COMPARISONS

Comparisons of holographic analyses between datasets obtained from different instruments are needed to assess the sources of noise, and to judge the reliability of the results. Helioseismic data from the recently-upgraded ground-based GONG+ network provides a natural source for comparison with the MDI observations. Currently, seismic images of the solar far side are updated daily on the MDI web site (<http://soi.stanford.edu/data/farside>), and have been helpful to a broad variety of users ranging from solar astronomers planning upcoming observing sessions to amateur radio enthusiasts. However, MDI is now exceeding its projected lifetime of six years. It is important to assess the ability of ground-based instrumentation, such as the GONG+ network, to continue the farside program, and other helioseismic projects, until new space-based instruments become available.

We performed similar holographic analyses of active regions observed both on the front and far sides of the Sun by the GONG+ network and the MDI instrument. The observations span a 24 hour time interval starting on 2001 September 29. GONG+ images made at the Big Bear, Learmonth, El Teide, and Cerro Tololo sites were used to achieve approximately 97 % temporal coverage. The GONG+ and MDI full-disk images were interpolated to form Postel's projections spanning approximately 60° , and tracked at the Carrington rotation rate. Figure 2 shows a comparison of the power spectra, integrated over temporal frequencies, ν , between 2 and 6 mHz. Of primary importance for local helioseismology is the sensitivity of the instruments to p -modes of high degree (ℓ). The fall-off of the power with ℓ observed in the GONG+ images, relative to that of MDI, clearly reflects the effects of atmospheric seeing and attenuation.

From both data sets, we computed phase-correlation

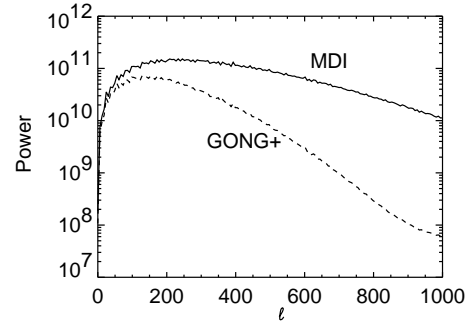


Figure 2. Power spectra made from 24 hr of simultaneous data from MDI and the GONG+ network. The solid line shows the MDI spectra, summed over temporal frequencies between 2 and 6 mHz and over all spatial directions, while the dashed line shows the spectra obtained from the GONG+ observations.

seismic images, sensitive to travel-time perturbations, using the methods described by Braun & Lindsey (2000b). In phase-correlation holography, we consider correlations between the egression and ingression:

$$C(\mathbf{r}, z, \nu) = H_+(\mathbf{r}, z, \nu)H_-^*(\mathbf{r}, z, \nu), \quad (2)$$

where the asterisk denotes the complex conjugate. The phase of the correlation is

$$\phi(\mathbf{r}, z) = \arg \left(\left\langle C(\mathbf{r}, z, \nu) \right\rangle_{\Delta\nu} \right), \quad (3)$$

where the brackets indicate an average over a bandwidth $\Delta\nu$. In the temporal domain, we may relate a mean travel-time difference, δt , between the egression and ingression to the correlation phase above by

$$\delta t(\mathbf{r}, z) = \phi(\mathbf{r}, z)/2\pi\nu_o, \quad (4)$$

where ν_o is the central frequency of the bandwidth $\Delta\nu$.

Depth diagnostics are achieved by using pupils similar to that shown in Figure 1, with the focal plane moved to various depths z below the surface. Figure 3 shows some sample images from this analysis, computed with p -modes over a 1 mHz bandwidth centered at 4 mHz. In general, the mean travel-time perturbations associated with the active regions shown here are sharpest at focal depths closest to the surface, and appear to defocus with depth. This is consistent with the ideas put forth by Braun & Lindsey (2000b), who suggest that most of the observed travel-time perturbations are confined to the surface and very likely due to a Wilson-like depression of the p -mode cavity in magnetic regions.

As Figure 3 illustrates, the travel-time images made with GONG+ appear noisier than the MDI images, especially for focal depths close to the solar surface. As the focus is moved downward, the acoustic radiation used to construct the images decreases in wavenumber. Below depths of approximately 10

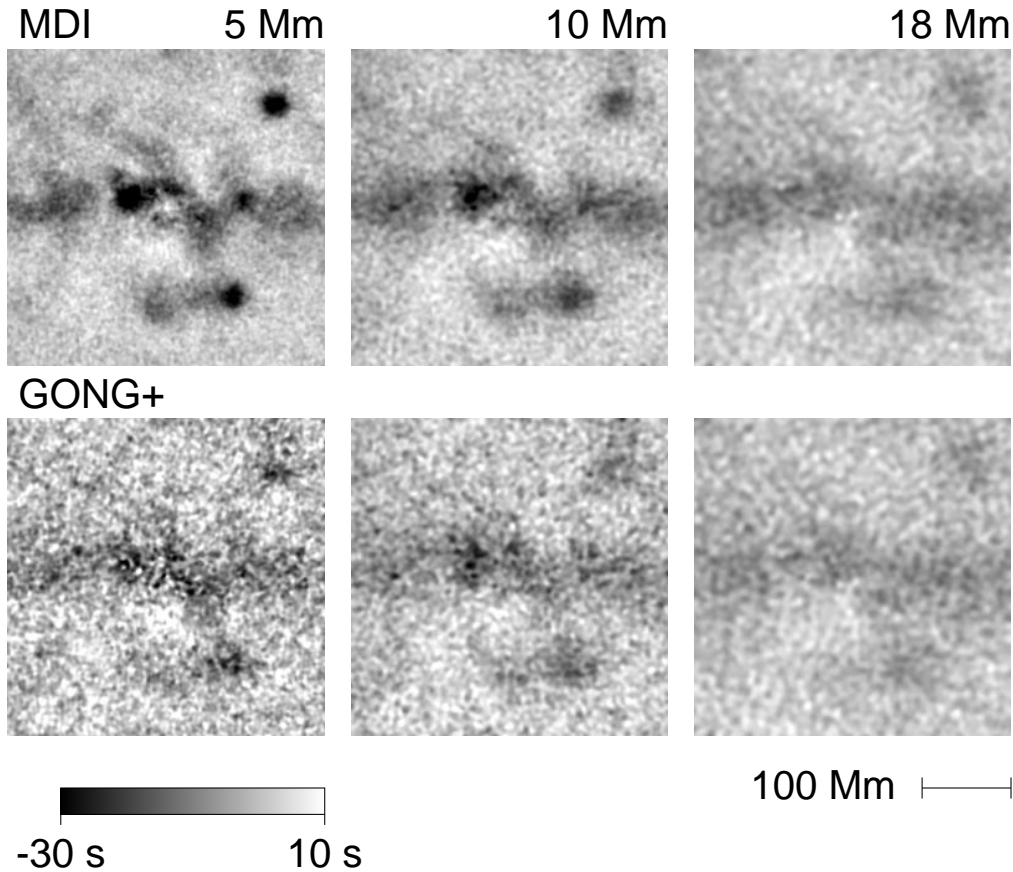


Figure 3. A comparison of phase-sensitive seismic images of the mean travel-time perturbations from data from the MDI onboard SOHO and from the GONG+ network, at three different depths of focus. The data were obtained from 24 hours of observations beginning 2001 September 29 and show the four sunspot groups NOAA AR 9633, 9634, 9636, and 9639. For these computations we used acoustic radiation over a 1 mHz bandwidth centered at 4 mHz.

Mm, propagating modes have wavenumbers (ℓ) below 300 and the phase-correlation travel-time images from GONG+ and MDI have similar noise characteristics. At this and lower depths, the similarity of the MDI and GONG-derived images demonstrates that the r.m.s. fluctuations in these images are solar in nature. At shallower depths, atmospheric seeing introduces excess noise, which increases with mode degree, to the images derived from GONG+ data.

Imaging the far side of the Sun was conceived as one of the first potential applications of helioseismic holography well over a decade ago (Lindsey & Braun, 1990). The successful application of phase-correlation holographic procedures to farside imaging (Lindsey & Braun, 2000a) introduced the immediate possibility of a synoptic monitor of far-side activity for purposes of space weather forecasting. This tool has long been needed for studies of active-region evolution as well. Our initial application of imaging the far surface of the Sun relied on what we call 2-skip/2-skip phase-sensitive holography. This scheme is essentially blind to active regions more than about 50 degrees from the antipode of disk center. Braun & Lindsey (2001) subsequently showed how travel-

time perturbations may be mapped over the entire portion of the Sun facing away from the Earth, including the polar regions. This is achieved by performing ingress–egression correlations computed over pupils illuminated by acoustic radiation which propagate one and three skips.

Images showing the acoustic travel-time perturbations over the entire far hemisphere obtained from the GONG+ and MDI data are essentially identical (Figure 4). This demonstrates that the GONG+ network may be used as the basis of a synoptic far-side imaging program of comparable quality to that now provided by MDI. The GONG+ project is now seeking resources to implement this program.

3. HORIZONTAL DOPPLER DIAGNOSTICS

Phase-correlation holography typically involves the assessment of travel-time perturbations derived from the observed temporal correlations between the egression and ingressions. Diagnostic procedures sensitive to flows may be developed in a variety of

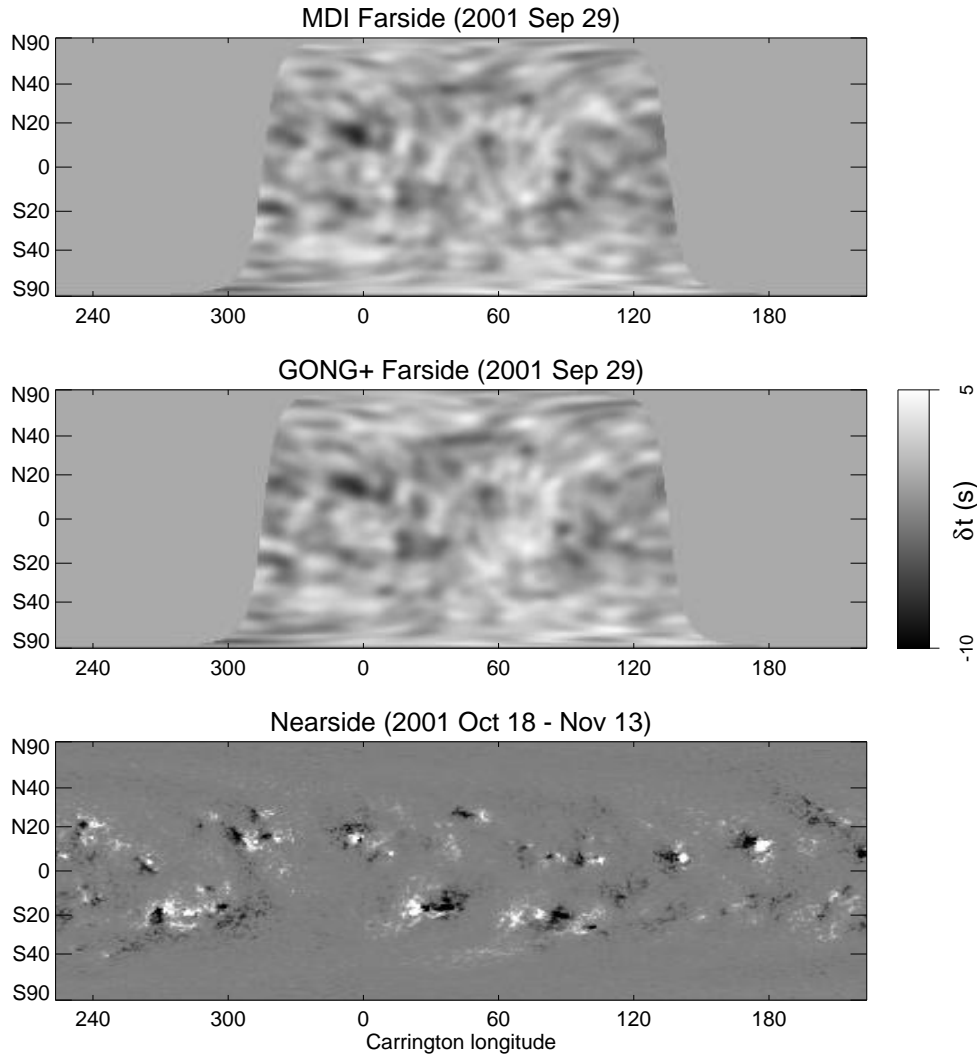


Figure 4. A comparison of seismic images of the solar far side made from data from the MDI and from the GONG+ network, and a synoptic magnetogram for the subsequent solar rotation. For farside imaging, we use p -modes with temporal frequencies between 2.5 and 4.5 mHz, and spherical harmonic degrees between 20 and 40.

ways. The method employed here divides the pupil P into four quadrants, each spanning 90 degrees and oriented in the North, South, East and West directions. Using just the North and South quadrants gives p -mode travel-times which are sensitive to wave advection caused by north or south motions. Likewise, the egressions and ingressions determined from the East and West quadrants are used to infer east-west motions. Denoting the quadrant's areas as N , S , E , and W , we compute the four egressions and four ingressions:

$$H_{\pm}^{N,S,E,W} = \int_{N,S,E,W} d^2\mathbf{r}' G_{\pm}(\mathbf{r}, \mathbf{r}', z, \nu) \psi(\mathbf{r}', \nu) \quad (5)$$

and compute the four correlations $C^{E \rightarrow W}$, $C^{W \rightarrow E}$, $C^{N \rightarrow S}$, and $C^{S \rightarrow N}$, where, for example,

$$C^{E \rightarrow W} = H_{+}^E H_{-}^{W*}, \text{ etc.} \quad (6)$$

(For convenience, we omit the arguments (\mathbf{r}, z, ν) , which are understood.) Defining four correlation phases, given by

$$\phi^{E \rightarrow W} = \arg \left(\left\langle C^{E \rightarrow W} \right\rangle_{\Delta\nu} \right), \text{ etc.,} \quad (7)$$

we interpret the phase-differences between opposite directions to be caused by horizontal flows:

$$V_x \propto -\frac{1}{2}(\phi^{E \rightarrow W} - \phi^{W \rightarrow E}), \quad (8)$$

$$V_y \propto -\frac{1}{2}(\phi^{S \rightarrow N} - \phi^{N \rightarrow S}). \quad (9)$$

Doppler-sensitive phase-difference images, when averaged over longitude, show the signatures of both differential rotation and meridional circulation with 24 hours of observations (Figure 5). We use published measurements of the photospheric differential rotation to calibrate Equations 8 and 9. Our simple calibration scheme assumes that the rotation rate does not change with depth over the range considered here, ignoring the gradients inferred by global helioseismology which are, at most, on the order of a few percent. Caution must be exercised in assessing and interpreting travel-time perturbations with observations that use uncorrected Doppler measurements over magnetic regions, due to phenomena which are now collectively called the “showerglass” (see Braun (1997); Lindsey & Braun (2002) and section 4 below). In this analysis, we simply mask out regions within sunspot umbrae and penumbrae, excluding completely their contribution to the holographic computations.

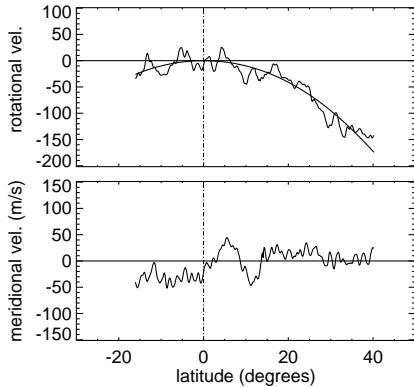


Figure 5. Averaging the E-W and N-S correlation phase signatures (at a focal depth of 7 Mm) over longitude shows clear evidence of differential rotation (top panel) and the meridional circulation (bottom panel) in 24 hours of observations. The velocity scale (y axis) is set by fitting the E-W correlation phase differences to published measurements of photospheric differential rotation (shown by the smooth curve in the top panel).

Figure 6 illustrates a sample of our results using MDI observations from the 24 hr period discussed in §2 above. We performed the analysis using p -modes at 3, 4, and 5 mHz, with 1 mHz bandwidths. All three sets of modes showed similar velocity fields, which were then combined by averaging to improve the statistics. Our Doppler-sensitive images generally reveal strong, localized outflows from sunspots, such as that around the spot group NOAA 9636 shown in Figure 6. These patterns strongly resemble the “moat” floats commonly observed in the photosphere (Brickhouse & LaBonte, 1988), which have similar magnitude (~ 500 m/s) and spatial extent. Similar outflows have also been previously seen in inversions of time-distance observations (Zhao, Kosovichev & Duvall, 2001). As Figure 6 shows, the velocity field derived with the focus placed below 10 Mm appears to be anticorrelated with the near surface field. In

general, the divergence images are all significantly correlated with the horizontal velocity divergence at the shallowest depth (3 Mm), with the correlation coefficient becoming negative below a depth of 10 Mm. We can quantitatively describe the behavior of the velocity divergence with depth by making scatter plots of the divergence values observed at a given depth with the (near-surface) value at 3 Mm depth. The “velocity ratio” is defined as the slope of a line fit to the scatter. The variation of the velocity ratio with the focus depth is shown in Figure 7.

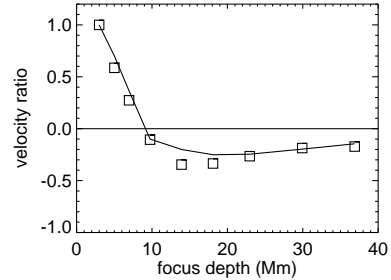


Figure 7. The velocity ratio is the slope of a linear fit to a scatter plot of the horizontal velocity-divergence image at a given depth to the divergence image at 3 Mm. The open squares are from the holographic observations, while the line connects values derived from a control computation in which the Doppler signatures at the surface are simply averaged over the pupil quadrants.

A major goal of our helioseismic Doppler diagnostics is to probe the variation with depth of flows caused by supergranulation and other convective effects. It is tempting to interpret the reversal of the horizontal divergence signal at 10 Mm as a subsurface “return-flow” in supergranule cells which penetrate below this depth. However, careful consideration shows that in fact, the reversal of the horizontal velocity patterns appears to be consistent with the expectations of a horizontal velocity pattern which is highly concentrated in the near-surface layers. As the focal plane is submerged, the pupils used in the holographic computations become more spatially extended (examples are shown in the middle three columns in Figure 8). The apparent reversal of the flows with depth may be caused by the increasing contribution of oppositely directed *surface* flows as the pupils increase in size. We test this hypothesis in the following fashion. Using the observed velocity field at 3 Mm as a best estimate of the actual surface field, we compute the weighted average of the surface velocity with each quadrant for every pupil employed in our holographic analysis. The weighting function is the same as that used in the egression and ingression computations (see § 8.1 of Lindsey & Braun (2000b)) Differences between the East and West, and North and South, quadrant averages provide estimates of the expected surface contribution (hereafter referred to as the “control”) to our seismic measurements. The divergence of the control velocities is shown in the right three panels in Figure 8.

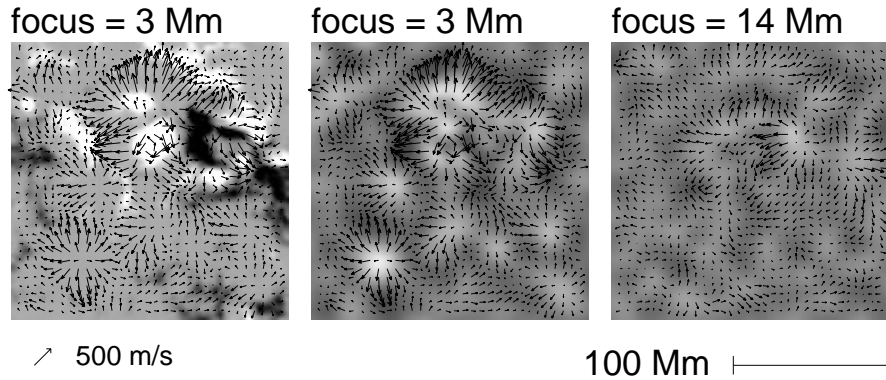


Figure 6. Horizontal Doppler diagnostics applied to 24 hr of data from MDI, which includes the major spot group in AR 9363. The left panel shows the observed velocity field, shown as vectors, for a focal depth of 3 Mm and superimposed on a magnetogram. The middle panel shows the same vector field shown in the first panel, but superimposed over an image of the horizontal divergence of the velocity. The right panel shows the velocity field and its divergence with the focal plane placed 14 Mm below the surface.

The control velocity patterns resemble the observations (left panels) to a high degree. We also computed velocity ratios for the control velocity fields in the same manner as performed for the seismic measurements. The slopes derived from the control are shown connected by a solid line in Figure 7, which are in remarkable agreement with the observed values (open squares).

4. THE SHOWERGLASS EFFECT

It is been known for some time that the photospheres in magnetic regions introduce strong local amplitude and phase perturbations in the acoustic wave field. The shifts in the phase due to surface magnetism act as a “showerglass” that makes the imaging of subsurface acoustic perturbations immediately below the showerglass particularly difficult, and sometimes impossible. In this section, we briefly summarize our recent progress in assessing the showerglass effect and developing a magnetic proxy that will permit its removal from the surface wave field prior to helioseismic imaging. The reader is referred to another paper in these proceedings which discusses these issues in more detail (Lindsey & Braun , 2002).

To assess the phase errors introduced by surface magnetic fields, we examine the statistics of the sets of correlations between the egressions (and ingressions), computed with the focal plane at the surface, and the local wave amplitude. These correlations are designed to compare an extrapolated acoustic field, propagated backward (or forward) in time from the measured egression (or ingression), with the actual surface wave field, and hence assess the local distortion in the latter due to surface activity. Plots of the mean phase and amplitude of these correlations, as functions of the surface magnetic flux density, are shown in Figure 9. The difference between the phases

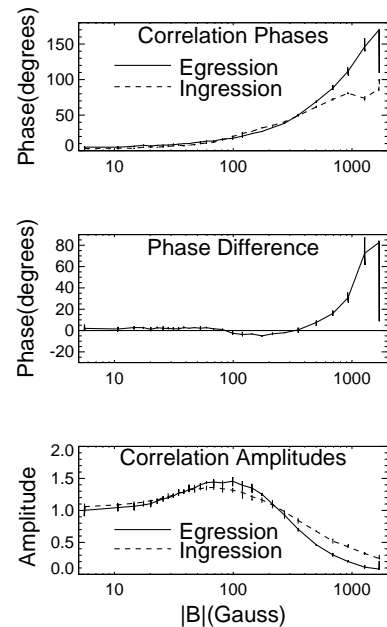


Figure 9. Correlations between the egression and ingression and local wave field as functions of the surface magnetic flux density. The top panel shows the phases of the correlations. The middle panel shows the difference in the phase between the egression and ingression correlations. The bottom panel shows the amplitudes of the correlations.

of the egression and ingression correlations at the strongest observed magnetic flux density is substantial, and correspond to travel-time perturbations on the order of 40 seconds or more between inward and outward propagating waves. This is comparable to the travel-time asymmetries in center-annuli correlations, centered on sunspots, reported previously by Duvall et al. (1996) and Braun (1997).

Where the phase errors are below a radian or so, the

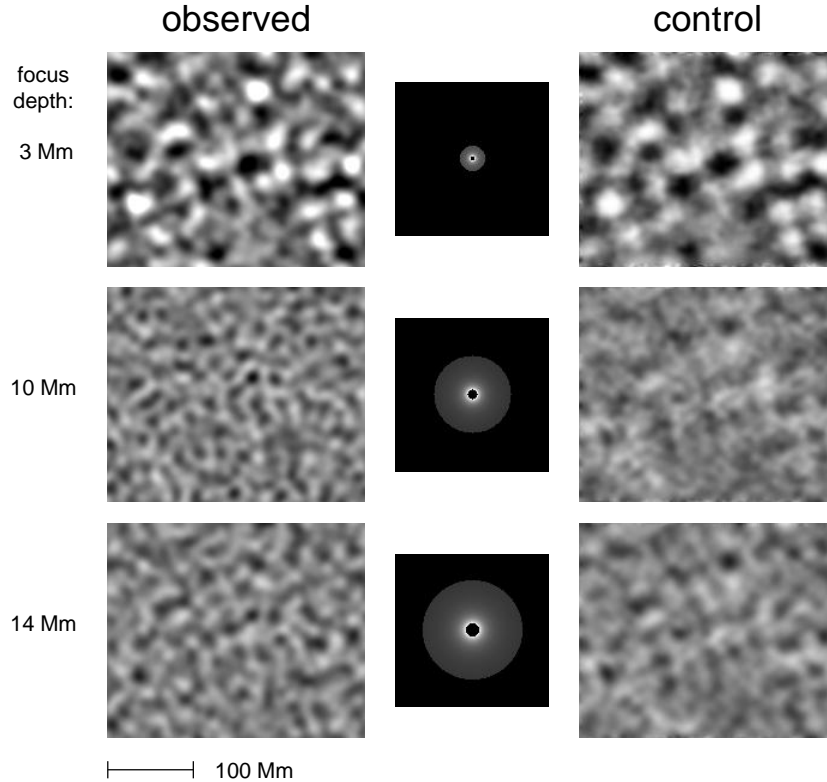


Figure 8. A comparison of the observed horizontal divergence, derived from seismic holography (left-most panels) with those derived from a control computation which assumes the Doppler signatures are concentrated at the solar surface (right-most panels). The middle panels show the weighted pupils used in the analysis.

Born approximation may be regarded as valid. In this case, it may be reasonable to consider modeling (e.g. inverting) uncorrected helioseismic data to reconstruct an acoustic perturbation which consists of both the surface showerglass and a (potentially more interesting) subsurface contribution. The regions below weak plages, for example, may be amenable to such modeling. However, given the strong perturbations introduced by active regions, we have found that the unambiguous detection of compact subsurface scatterers within 10 Mm or less below magnetic regions requires a careful assessment and removal of the phase errors introduced at the surface. We have recently begun to explore the use of the observed magnetic flux density as a proxy for the phase errors, using measurements of the egression and ingression correlations like those shown in Figure 9. Preliminary results are encouraging, and include the discovery of compact features below large active regions, some of which are invisible or degraded in seismic images in which the showerglass is not removed.

5. CONCLUSIONS

This report represents a snapshot of our recent research efforts in a variety of local helioseismic topics. Our main findings may be summarized as follows:

- Helioseismic images of the far side obtained with data from the GONG+ network are essentially identical to those obtained with the MDI instrument, supporting the proposal to add a synoptic farside imaging program to the GONG+ project.
- Comparisons of seismic imaging applied to simultaneous GONG+ and MDI data suggest that GONG+ data is well suited for local helioseismic analysis, particularly at depths of 10 Mm and deeper below the convection zone.
- Doppler-sensitive holography shows supergranulation flows and outflows from sunspots, consistent with surface measurements, and most likely confined to the near-surface layers of the convection zone.
- Correlations between the local acoustic wave field and the extrapolated egression and ingressions demonstrate the existence of an “acoustic showerglass” in magnetic regions, which severely scrambles the phase of impinging radiation. The removal of the showerglass by means of a magnetic proxy appears crucial in the identification and modeling of compact acoustic scatterers below active regions.

Further information and reprints of recent articles on our program in local helioseismology may be found at <http://colorado-research.com/~dbraun>.

ACKNOWLEDGMENTS

We dedicate this effort to the memory of our friend and colleague, Karen Harvey. Charles Lindsey worked under the sponsorship of the Solar Physics Research Corporation during most of the period of this research. This work is supported by grants from the Stellar Astronomy and Astrophysics Program at the National Science Foundation, and the Sun-Earth Connection Living With A Star and SR&T Programs at the National Aeronautics and Space Administration. This work uses data from the GONG+ Network and the MDI instrument on *SOHO*. *SOHO* is a project of international cooperation between ESA and NASA. The GONG project is managed by the National Solar Observatory, which is operated by AURA, Inc. under a cooperative agreement with the National Science Foundation. The data were acquired by instruments operated by the Big Bear Solar Observatory, High Altitude Observatory, Learmonth Solar Observatory, Udaipur Solar Observatory, Instituto de Astrofísica de Canarias, and Cerro Tololo Interamerican Observatory.

REFERENCES

- Braun D.C. 1997, ApJ 487, 447
 Braun D.C., Lindsey C., 2000a, Sol. Phys. 192, 285
 Braun D.C., Lindsey C., 2000b, Sol. Phys. 192, 307
 Braun D.C., Lindsey C., 2001, ApJ 560, L189
 Brickhouse, N.S., LaBonte, B.J. 1988, Sol. Phys. 115, 43
 Duvall, T.L.Jr, D'Silva, S., Jefferies, S.M., et al. 1996, Nature 379, 235
 Lindsey C., Braun D.C., 1990, Sol. Phys. 126, 101
 Lindsey C., Braun D.C., 2000a, Science 287, 1799
 Lindsey C., Braun D.C., 2000b, Sol. Phys. 192, 261
 Lindsey C., Braun D.C., 2002, (these proceedings)
 Zhao, J., Kosovichev, A.G., Duvall, T.L., Jr., 2001, ApJ 557, 384